Selective CO_2-to-C_2H_6 photoconversion over the electron-rich Au anchored on In_2O_3 nanosheets

Bangwang Li,[†a] Youbin Zheng,[†a] Shengyue Zhang,[a] Zihan Qin,[a] Xiangning Wang,[a] Siying Liu,[a] Mingyu Wu,[a] Yaping Li,[b] Shangming He,[*c] Yongfu Sun,[*a] and Yi Xie[a]

a. Hefei National Research Center for Physical Sciences at Microscale, University of Science and Technology of China, Hefei 230026, China.

b. Center for Micro- and Nanoscale Research and Fabrication, University of Science and Technology of China, Hefei 230026, China.

c. Shanghai Synchrotron Radiation Facility (SSRF), Shanghai Advanced Research Institute (SARI), and Shanghai Institute of Applied Physics, Chinese Academy of Sciences (CAS), Shanghai 201204, China.

†Bangwang Li and Youbin Zheng contributed equally to this work.

*E-mail: yfsun@ustc.edu.cn, hesm@sari.ac.cn

Material

$InCl_3 \cdot 4H_2O$ (AR), $HAuCl_4 \cdot 4H_2O$ (AR), L(+)-Ascorbic acid (AR), KBr (SP) and NaOH (AR) were purchased from Sinopharm Chemical Reagent Co., Ltd.. Polyvinylpyrrolidone K30 (PVP, GR) was purchased from Beijing Vokai Biotechnology Co., LTD.. The water used was ultrapure (18.25 MΩ cm) and generated by water purifier (WP-UP-1810). All chemicals were used without further purification.

Method

Synthesis of In_2O_3 nanosheets

In a typical synthetic procedure, 1 mmol $InCl_3$ was added to 40 mL deionized H_2O under constant magnetic stirring for 10 min, after that the 60 mL 0.1 M NaOH solution prepared in advance was slowly added. Then, the above solution was kept stirring for 5 h, allowing to stand for 30 min for phase separation. The obtained white bottom sediment was collected by centrifuging, washed with H_2O for several times, and then dried in vacuum overnight. Finally, the as-obtained precursor was rapidly heated to 400 °C in air by the the custom-made ultra-fast heating furnace (Hefei In-situ Technology. Co., Ltd.) and kept at the temperature for 3 min. After cooling to room temperature, the In_2O_3 nanosheets were collected for further characterization.

Synthesis of Au/In_2O_3 nanosheets

In a typical procedure, 100 mg of In_2O_3 nanosheets were initially dispersed into 10 mL of deionized water by continuous stirring and heated at 353 K. Then, a certain amount of $HAuCl_4 \cdot 4H_2O$ aqueous solution was added. After stirring for 30 min, 105 mg of PVP, 120 mg of L(+)-Ascorbic acid and 300 mg of KBr were added. The mixture was kept stirring for 3 h at 353 K. The products were collected by centrifugation, washed with deionized water for three times and dried at 333 K overnight. The obtained products were stored in a vacuum vessel for further characterization.

Characterization

XRD patterns were carried on the Philips X'Pert Pro Super diffractometer with Cu Kα radiation (λ = 1.54178 Å). X-ray photoelectron spectroscopy (XPS) was obtained from a Thermo ESCALAB 250Xi with Al Kα ($h\nu$ = 1,486.6 eV) as the excitation source. Transmission electron microscopy (TEM) images were taken using a JEM-2100 Plus at 200 kV. High-resolution transmission electron microscopy (HRTEM) images and the energy dispersive spectroscopy (EDS) mapping analyses was performed on a JEOL-F200. Aberration-corrected high-angle annular dark-field scanning transmission electron microscopy (AC HAADF-STEM) images were recorded on a JEM-ARM200F with a spherical aberration corrector. UV-vis diffuse reflectance spectroscopy (UV-vis DRS) was recorded on a UV/Vis-NIR spectrophotometer (Perkin Elmer Lambda 950). Metal content was determined by inductively coupled plasma atomic emission spectroscopy (ICP-AES, PerkinElmer Optima 7300 DV). Photoluminescence (PL) spectra were obtained by horiba Fluorolog-3-Tau and deltaflexith with an excitation wavelength at 325 nm. *In situ* Fourier-transform infrared spectroscopy (FTIR) was measured on a Thermo Scientific Nicolet iS50. *In situ* EPR spectra were recorded on a JEOL JES-FA200 spectrometer. Photoelectrochemical measurements were performed in a three-electrode system at an CHI660E electrochemical station. TPD measurements were performed on a Micromeritics ChemiSorb 2920

analyzer equipped with a thermal conductivity detector (TCD). XAFS spectra at the In K-edge and the Au L_3-edge of samples in transition mode were collected at the BL13SSW and the BL20U1 beamline in the Shanghai Synchrotron Radiation Facility (SSRF). Synchrotron-radiation vacuum ultraviolet photoionization mass spectrometry (SVUV-PIMS) was carried out at the BL03U beamline in National Synchrotron Radiation Laboratory, Hefei, China (NSRL). Synchrotron-radiation ultraviolet photoelectron spectroscopy (UPS) and *in situ* XPS measurement were measured at the BL11U beamline in NSRL. The work function (WF) was obtained by the difference between the photon energy and the binding energy of the secondary cutoff edge. To be exact, WF = $h\nu$ - (E_{cutoff} - E_F), E_B = $h\nu$ - (E_K + 4.3 - 5.0), (E_B: binding energy, $h\nu$ is the incident photon energy, E_K is kinetic energy, E_{cutoff} is secondary cutoff edge and E_F is Fermi level). Photon energy was 50.0 eV and a sample bias of -5 V was applied to observe the secondary electron cutoff.

XAFS measurements

In K-edge EXAFS data were collected on the BL13SSW beamline at the Shanghai Synchrotron Radiation Facility (SSRF) using the top-up mode operation with a ring current of 220 mA at 3.5 GeV. A 13-pole wiggler with the maximum magnetic field of 1.5 T inserted in the straight section of the storage ring was applied. XAFS data were tested by a fixed-exit double-crystal Si (311) monochromator. The photon flux at the sample position was 2.3×10^{11} photons/s and the incident energy was set as 27.9 keV for In. For each grazing incident angle, X-ray absorption spectra were recorded by using an N_2/Ar mixed-gas-filled ionization chamber and passivated implanted planar silicon (Canberra Co.) for the incident and fluorescent X-ray photons, respectively. The raw data was analyzed by IFEFFIT software package based on the standard data analysis procedures. The energy calibration was performed with In_2O_3 powder reference using the Athena package.

Au L_3-edge XAFS measurements were collected at the BL20U1 in Shanghai Synchrotron Radiation Facility (SSRF). The applied electron beam energy was 3.5 GeV and the stored current was 220 mA (top-up). A hard X-ray branch of the E-line, providing a photon flux of 2×10^{12} photons/s at 11.9 keV, was constructed using 24-pole in-vacuum undulators. For each grazing incident angle, X-ray absorption spectra were recorded by using an N_2/Ar mixed-gas-filled ionization chamber and passivated implanted planar silicon (Canberra Co.) for the incident and fluorescent X-ray photons, respectively. The raw data was analyzed by IFEFFIT software package based on the standard data analysis procedures. The energy calibration was performed with Au foil reference using the Athena package.

***In situ* XPS measurements**

Synchrotron-radiation *in situ* XPS measurements were recorded at the photoemission end-station at beamline BL11U in the NSRL in Hefei, China. The endstation has three chambers that are composed of an analysis chamber, a preparation chamber, as well as a load-lock chamber. The analysis chamber is linked to the beamline with a VG Scienta R4000 electron energy analyser. In this work, the samples were transferred to the analysis chamber for XPS measurement. Then, the preparation chamber can be vacuuized until the pressure was down to $< 10^{-9}$ mbar for sample transfer. Last, the samples were transferred to the analysis chamber for *in situ* XPS testing under the dark and light irradiation.

***In situ* FTIR measurements**

In situ FTIR spectra were performed on Thermo Scientific Nicolet iS50, which was equipped with an MCT detector cooled by liquid nitrogen. In particular, as for CO_2 photoreduction, the sample was degassed in Ar atmosphere for 30 min, and then the gas flow was changed to pure CO_2 with H_2O vapor for adsorption at room temperature. The background spectrum was obtained after 30 min of adsorption in CO_2 atmosphere. After switching on the light, *in situ* FTIR spectra were recorded without break for 10 min.

***In situ* EPR measurements.**

In situ EPR spectra were recorded on a JEOL JES-FA200 spectrometer at ambient temperature. For the detection of superoxide radical ($\cdot O_2^-$), 8 mg of the samples were dispersed in 900 μL of methyl alcohol by ultrasound for 1 min, and then 100 μL of dilute DMPO solution was added. The mixture was placed in JEOL JES-FA200 ESR spectrometer for further testing in the dark or irradiation condition, and the same Xe lamp was utilized in the EPR tests. For the detection of hydroxyl radical (·OH), the same procedure was followed, except for substituting methyl alcohol with deionized water.

Photocatalytic CO_2 reduction measurement

In the typical CO_2 photocatalytic reduction process, 5 mg of the obtained Au/In_2O_3 powders were initially dispersed in 1 mL of deionized H_2O and then the dispersions were dripped onto the circular quartz glass with 4 cm diameter which was treated at 50 ℃ for 30 min to evaporate the water. After that, the quartz glass was vertically placed in the reaction cell with 2 mL of deionized H_2O. Afterwards, the reaction cell was vacuum-treated three times to remove air and high-purity CO_2 gas mixture was introduced to reach atmospheric pressure with irradiated by a 300 W Xe lamp (CEL-HXF300, Beijing China Education Au-light Co., Ltd.). During the process of light irradiation, the gas products were qualitatively detected by Techcomp GC8860 gas chromatograph (FID detector, TDX-01 column). When a new catalytic cycle began, the reactor was degassed and refilled with high-purity CO_2.

DFT calculation details

The first-principles calculations were performed with the Vienna *ab initio* simulation package (VASP).[1] The interaction between ions and valence electrons was described using projector augmented wave (PAW) potentials, and the exchange-correlation interaction between electrons was treated using the generalized gradient approximation (GGA) in the Perdew-Burke-Ernzerhof (PBE) form.[2] Here 2 × 2 × 1 Monkhorst-Pack K mesh and 480 eV cutoff energy were applied for structure relaxation, while 5 × 5 × 1 Monkhorst-Pack K mesh and 480 eV cutoff energy were applied for density of statue and charge density calculation. The ionic relaxations for all structures in the calculations were carried out under the conventional energy (10^{-5} eV) and force (0.015 eV $Å^{-1}$) convergence criteria. The crystal orbital Hamilton population (COHP) results here were obtained by LOBSTER.[3-8] The metal oxide slab along the defined projection was built with 1.5 nm vacuum layer to avoid interactions.

The plane-averaged charge density was obtained by the following equation,

$\sigma(z)=\iint\rho(\mathbf{r})dxdy$

where $\rho(\mathbf{r})$ is the charge density obtained from the self-consistent field calculation, and $\sigma(z)$ is

the as-obtained plane-averaged charge density.

Gibbs free energies for each gaseous and adsorbed species were calculated at 298.15 K, according to the expression,

$G = E_{DFT} + E_{ZPE} - TS + pV - \Delta U(0 \rightarrow T)$

where E_{DFT} is the electronic energy calculated for specified geometrical structures, E_{ZPE} is the zero-point energy, S is the entropy, T is the temperature which is set to 298.15 K here, pV is the volume work, $\Delta U(0 \rightarrow T)$ is the phonon contribution to the internal energy change from 0 K to temperature T. We treated the charge of the system refer to the widely-recognized computational hydrogen electrode (CHE) mode,[9] in which each reaction step was regarded as a simultaneous transfer of the proton-electron pair as a function of the applied potential. Thus, free energy changes relative to an initial state of gaseous CO_2 free above an empty surface can be represented by:

$\Delta G [*CO_2] = G [*CO_2] - (G [*] + G [CO_2])$

$\Delta G [*COOH] = G [*COOH] - (G [CO_2*] + G [H^+ + e^-])$

$\Delta G [*CO] = (G [*CO] + G [H_2O]) - (G [*COOH] + G [H^+ + e^-])$

$\Delta G [*CHO] = G [*CHO] - (G [*CO] + G [H^+ + e^-])$

$\Delta G [*CH_2O] = G [*CH_2O] - (G [*CHO] + G [H^+ + e^-])$

$\Delta G [*CH_2OH] = G [*CH_2OH] - (G [*CH_2O] + G [H^+ + e^-])$

$\Delta G [*CH_2] = (G [*CH_2] + G [H_2O]) - (G [*CH_2OH] + G [H^+ + e^-])$

$\Delta G [*CH_3] = G [*CH_3] - (G [*CH_2] + G [H^+ + e^-])$

$\Delta G [* + CH_4] = (G [CH_4] + G [*]) - (G [*CH_3] + G [H^+ + e^-])$

$\Delta G [*COCO] = G [*COCO] - (G [*CO] + G [CO])$

$\Delta G [*COCOH] = G [*COCOH] - (G [*COCO] + G [H^+ + e^-])$

$\Delta G [*COC(H)OH] = G [*COCOH_2] - (G [*COCOH] + G [H^+ + e^-])$

$\Delta G [*COCH] = (G [*COCH] + G [H_2O]) - (G [*COC(H)OH] + G [H^+ + e^-])$

$\Delta G [*COCH_2] = G [*COCH_2] - (G [*COCH] + G [H^+ + e^-])$

$\Delta G [*COHCH_2] = G [*COHCH_2] - (G [*COCH_2] + G [H^+ + e^-])$

$\Delta G [*C(H)OHCH_2] = G [*C(H)OHCH_2] - (G [*COHCH_2] + G [H^+ + e^-])$

$\Delta G [*CHCH] = (G [*CHCH] + G [H_2O]) - (G [*C(H)OHCH_2] + G [H^+ + e^-])$

$\Delta G [*CHCH_2] = G [*CHCH_2] - (G [*CHCH] + G [H^+ + e^-])$

$\Delta G [*CH_2CH_2] = G [*CH_2CH_2] - (G [*CHCH_2] + G [H^+ + e^-])$

$\Delta G [*CH_2CH_3] = G [*CH_2CH_3] - (G [*CHCH_3] + G [H^+ + e^-])$

$\Delta G [* + CH_3CH_3] = G [* + CH_3CH_3] - (G [*CH_2CH_3] + G [H^+ + e^-])$

$G [H^+ + e^-] = 1/2 \times G[H_2] - eU$

where * is the substrate, U is the applied overpotential and e is the elementary charge. In this study, U = 0 V versus reversible hydrogen electrode.

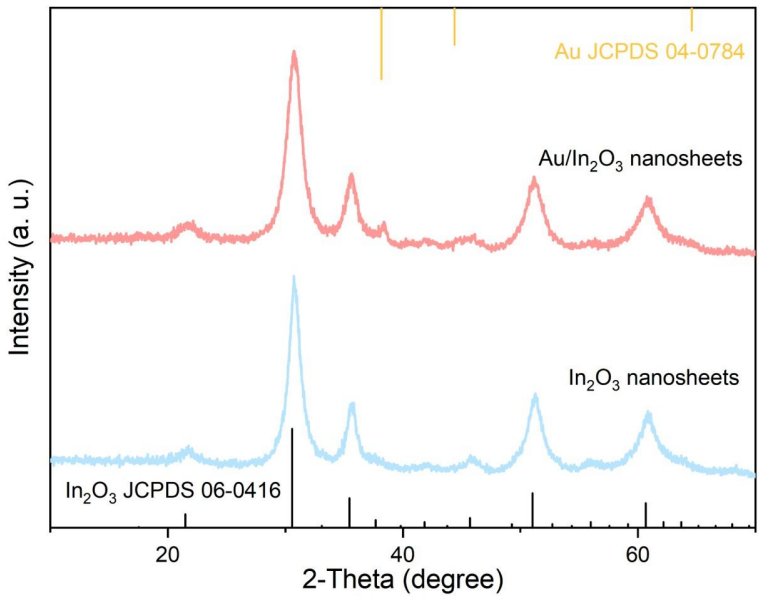

Fig. S1. XRD patterns of the Au/In_2O_3 nanosheets and the In_2O_3 nanosheets.

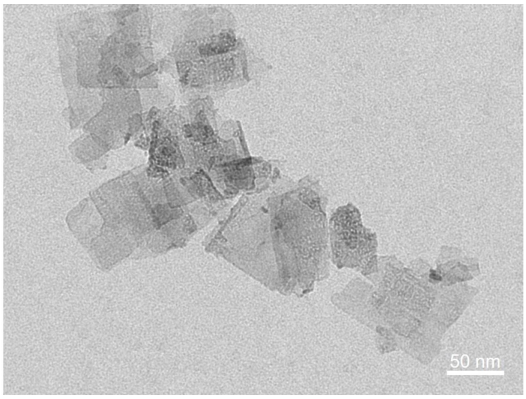

Fig. S2. TEM image of the In_2O_3 nanosheets.

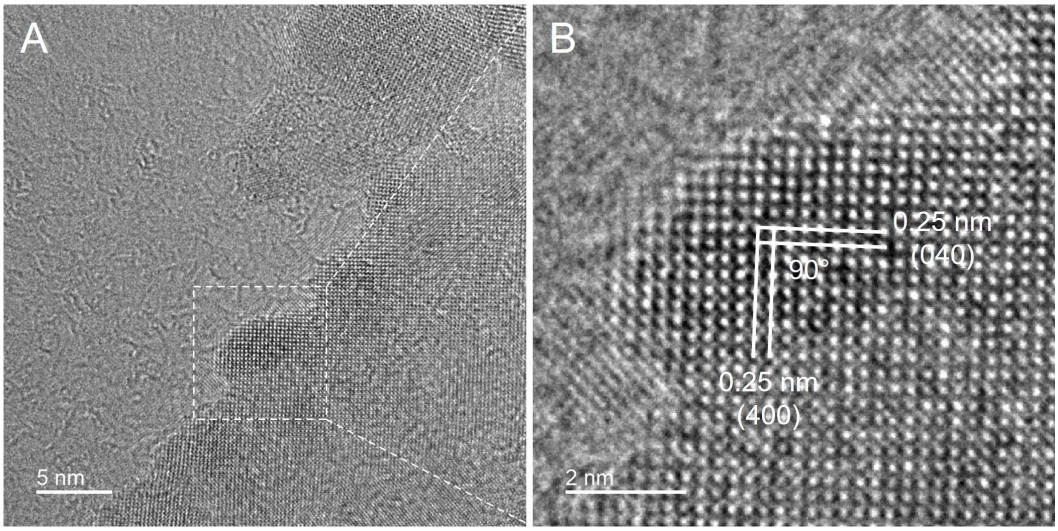

Fig. S3. (A) HRTEM image and (B) the corresponding enlarged HRTEM image of the In_2O_3 nanosheets.

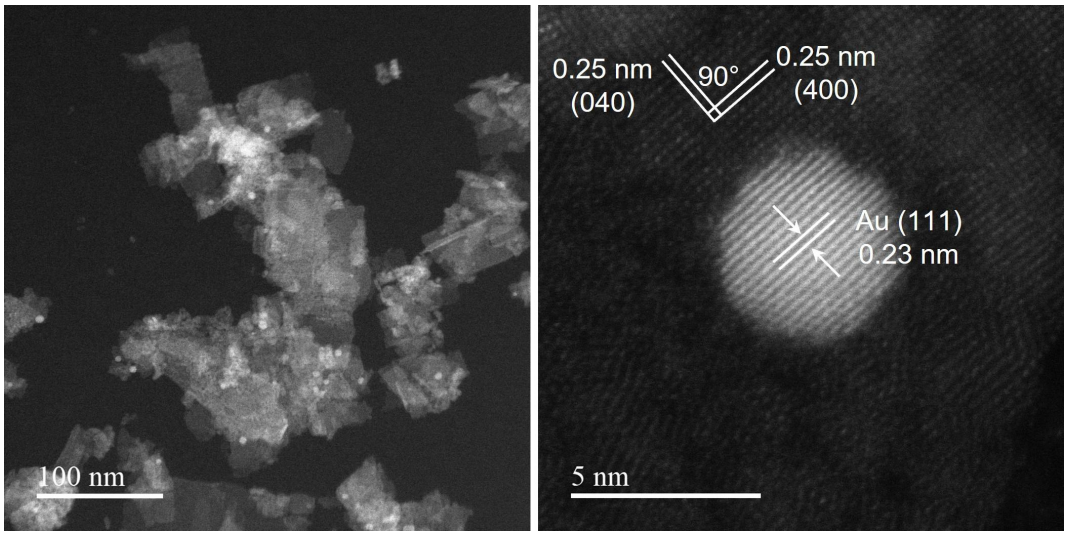

Fig. S4. AC HAADF-STEM images of the Au/In_2O_3 nanosheets.

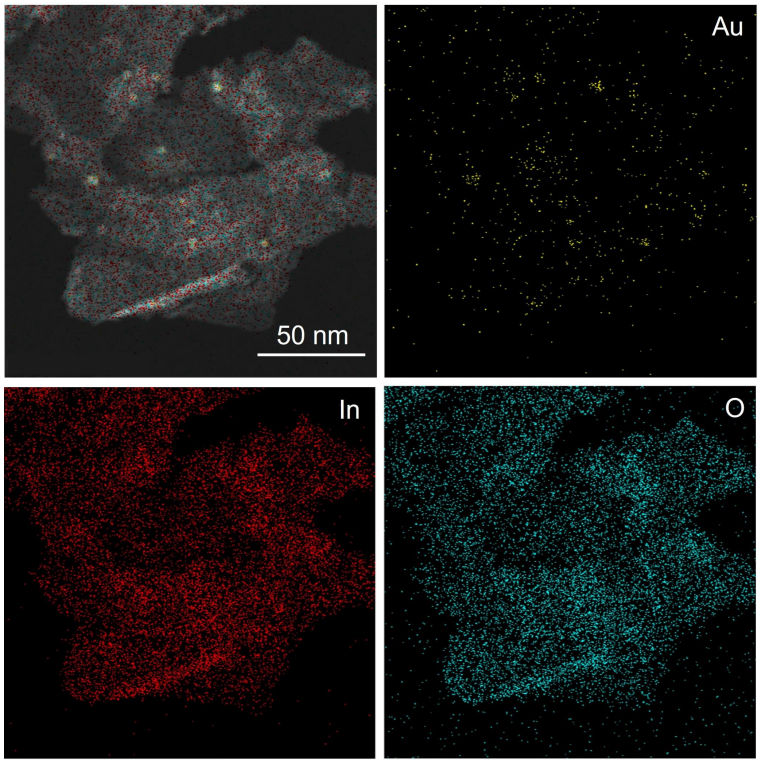

Fig. S5. EDS mapping images of the Au/In_2O_3 nanosheets.

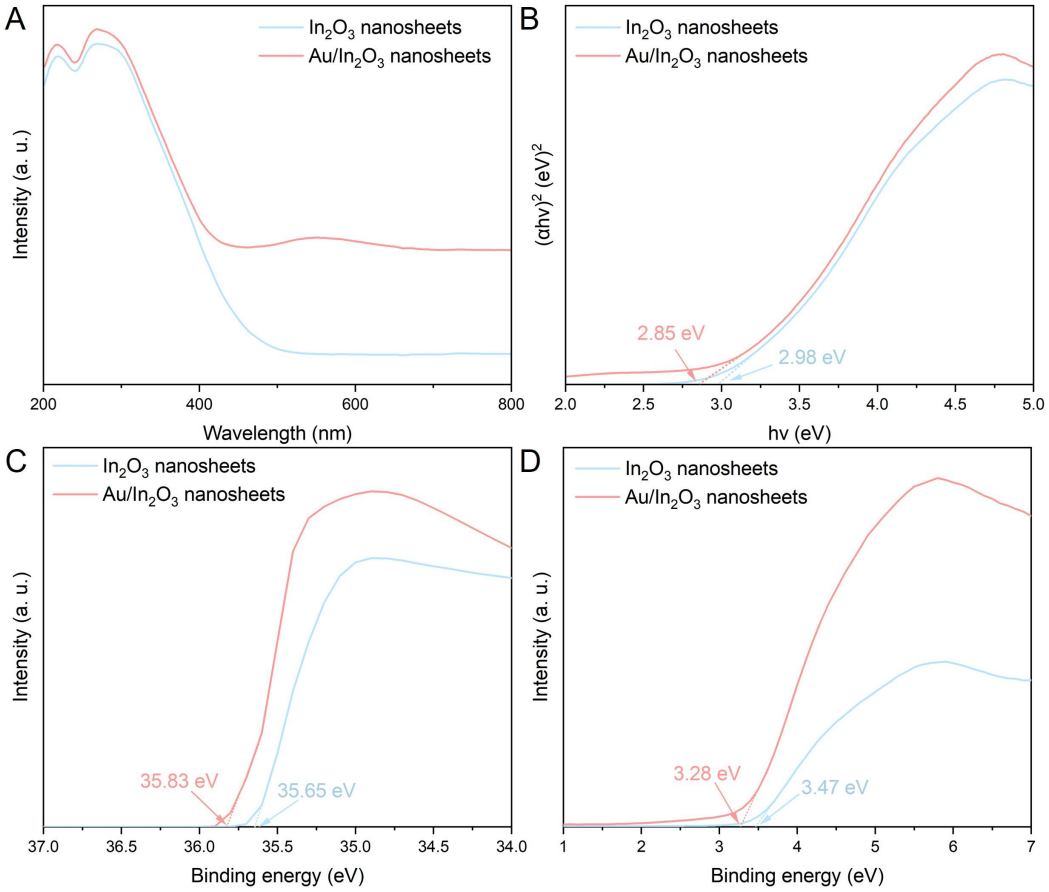

Fig. S6. (A) UV-vis diffuse reflectance spectra, (B) the band gaps estimated by a related curve of $(\alpha h\upsilon)^2$ versus photon energy plotted based on UV-vis diffuse reflectance spectra (the Tauc plots), (C) the secondary electron cutoff energy measured by SRPES spectra and (D) the valence band spectra of the Au/In_2O_3 nanosheets and the In_2O_3 nanosheets.

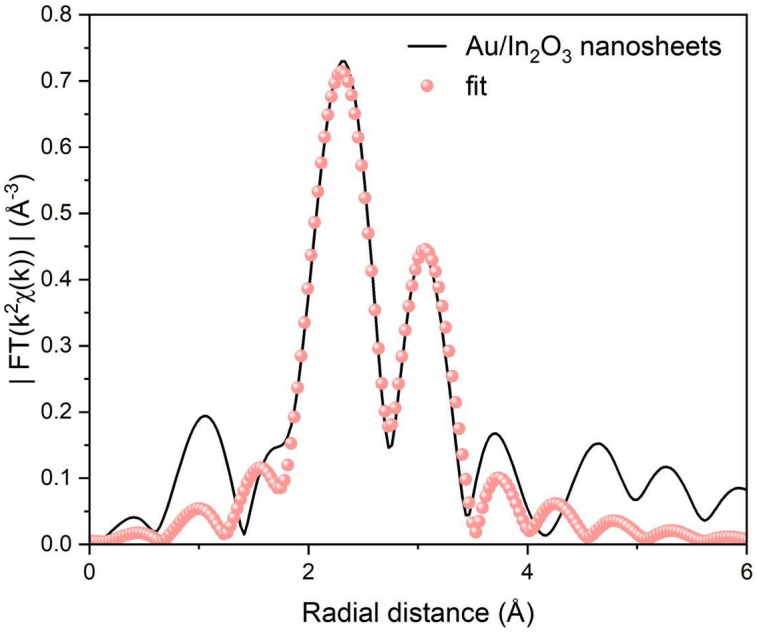

Fig. S7. Fourier transforms of EXAFS of the Au L_3-edge and fitting of the Au/In_2O_3 nanosheets.

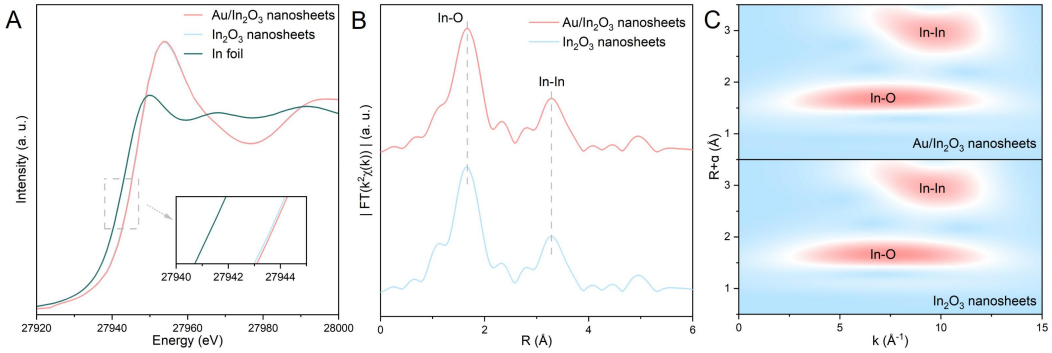

Fig. S8. (A) XANES spectra of In K-edge (B) k^2-weighted FT-EXAFS spectra and (C) WT-EXAFS spectra for the Au/In_2O_3 nanosheets, the In_2O_3 nanosheets and In foil. The In foil standard data was from SSRF database.

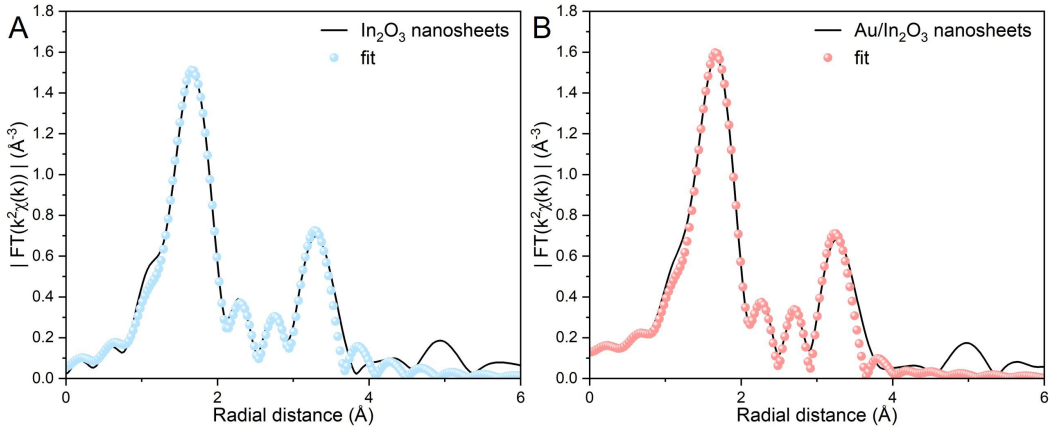

Fig. S9. Fourier transforms of EXAFS of the In K-edge and fitting of (A) the In_2O_3 nanosheets and (B) the Au/In_2O_3 nanosheets.

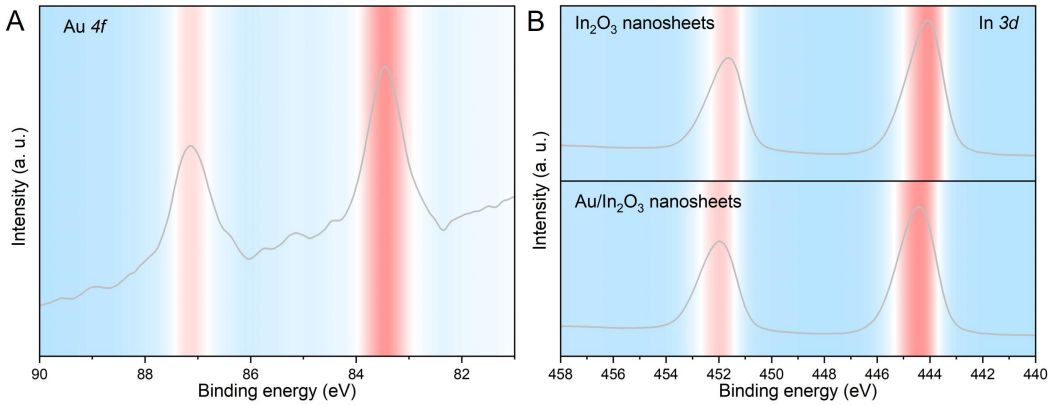

Fig. S10. (A) Au *4f* XPS spectrum of the Au/In_2O_3 nanosheets and (B) In *3d* XPS spectra of the Au/In_2O_3 nanosheets and the In_2O_3 nanosheets.

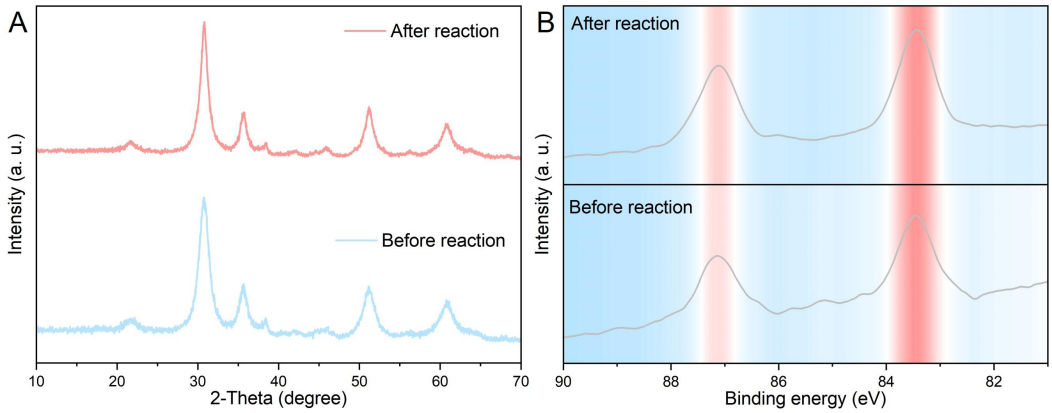

Fig. S11. (A) XRD patterns of the Au/In_2O_3 nanosheets before and after cycle tests. (B) Au *4f* XPS spectra of the Au/In_2O_3 nanosheets before and after cycle tests. The XRD patterns and Au *4f* XPS spectra before reaction could also be indexed to Fig. S1 and Fig. S10A, respectively.

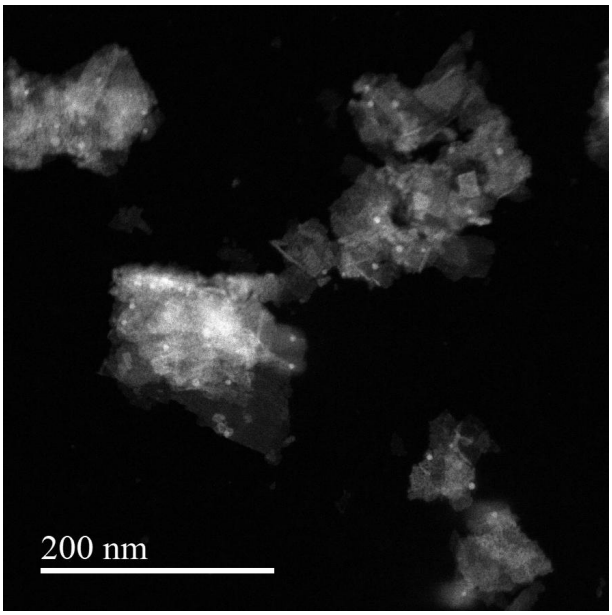

Fig. S12. AC HAADF-STEM image of the Au/In_2O_3 nanosheets after cycle tests.

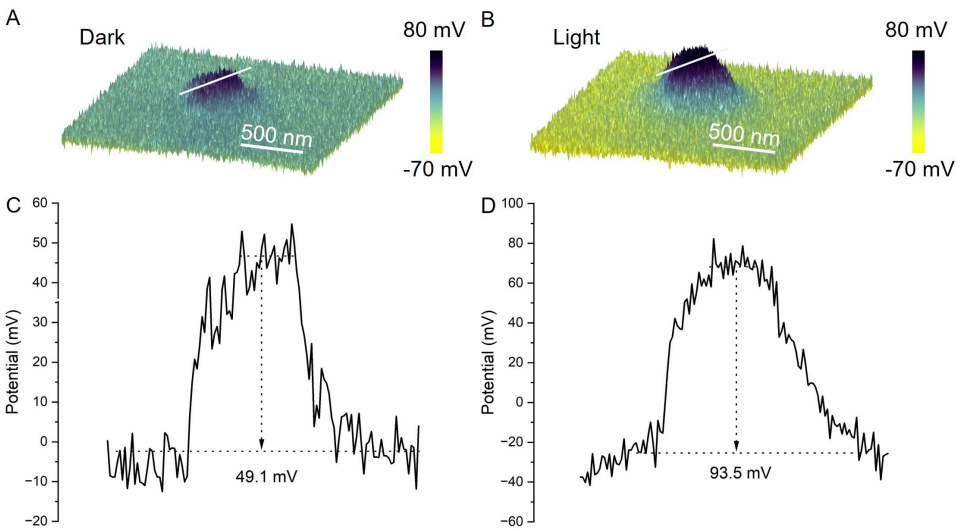

Fig. S13. *In situ* KPFM images of the In_2O_3 nanosheets (A) in the dark and (B) under illumination. (C, D) The corresponding line scan potential amplitudes along the white line marked in (A, B).

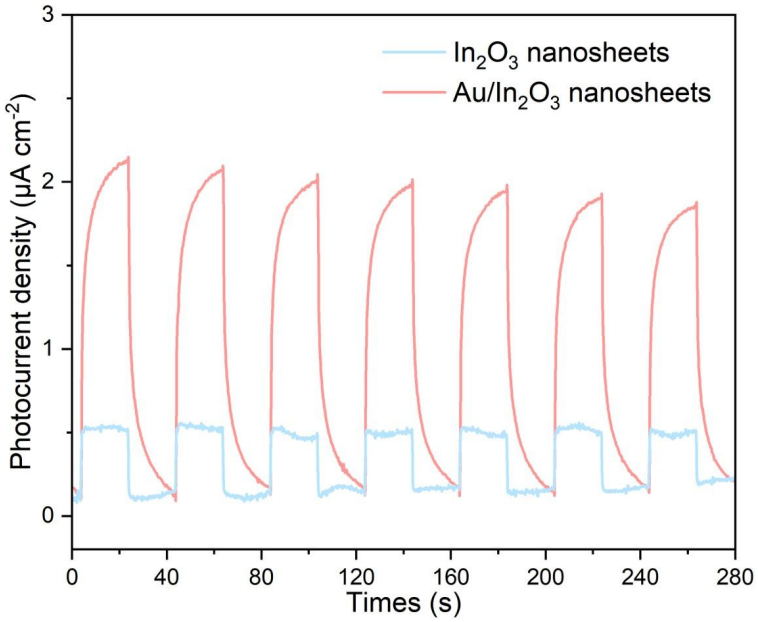

Fig. S14. Photocurrent intensity of the Au/In_2O_3 nanosheets and the In_2O_3 nanosheets.

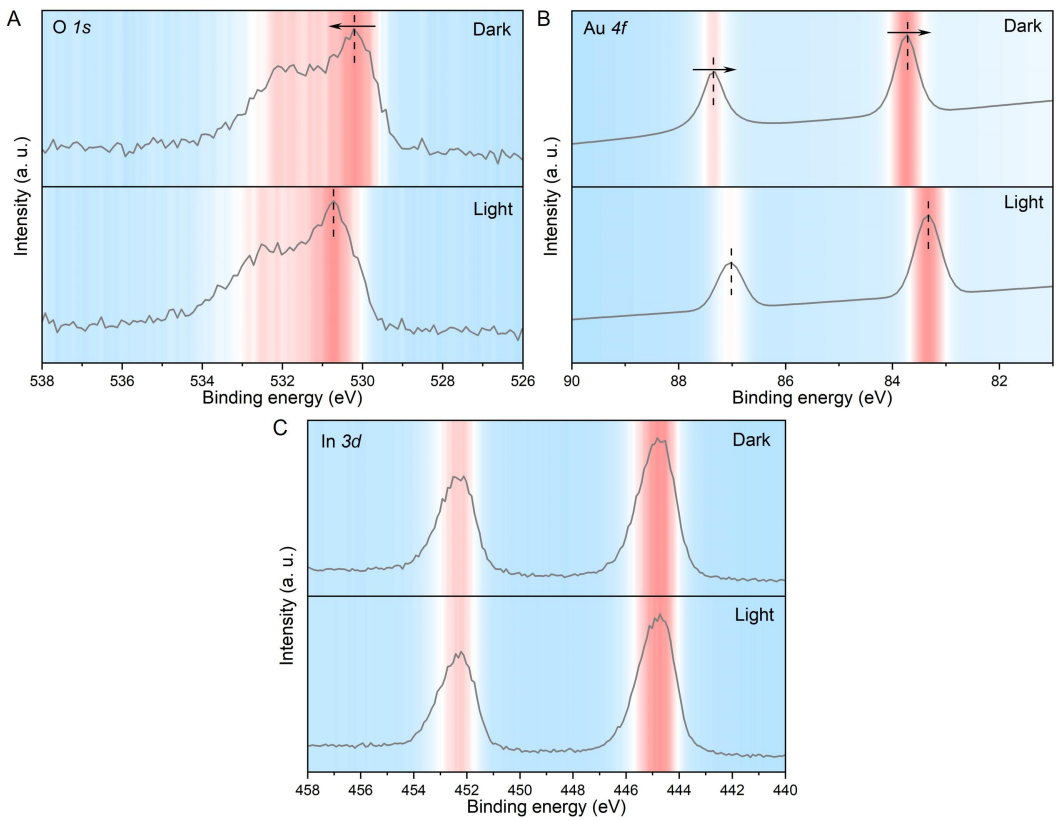

Fig. S15. (A) *In situ* O *1s* XPS spectra, (B) *in situ* Au *4f* XPS spectra and (C) *in situ* In *3d* XPS spectra over the Au/In_2O_3 nanosheets.

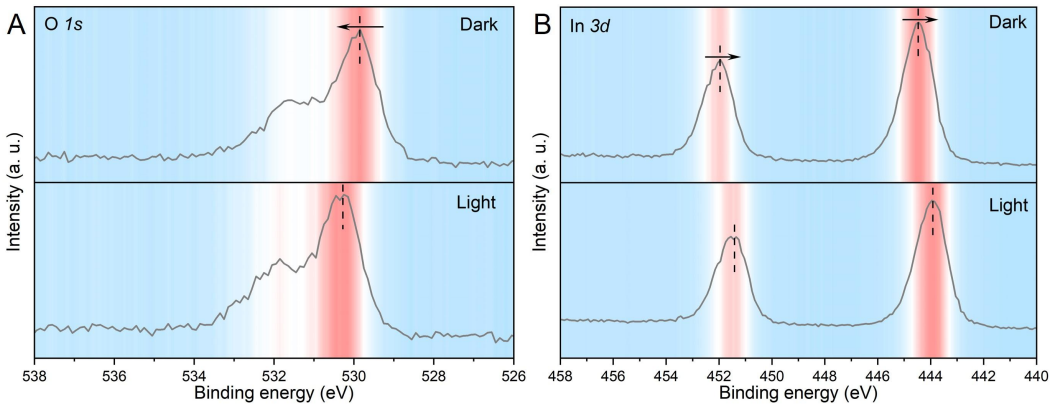

Fig. S16. (A) *In situ* O *1s* XPS spectra and (B) *in situ* In *3d* XPS spectra over the In_2O_3 nanosheets.

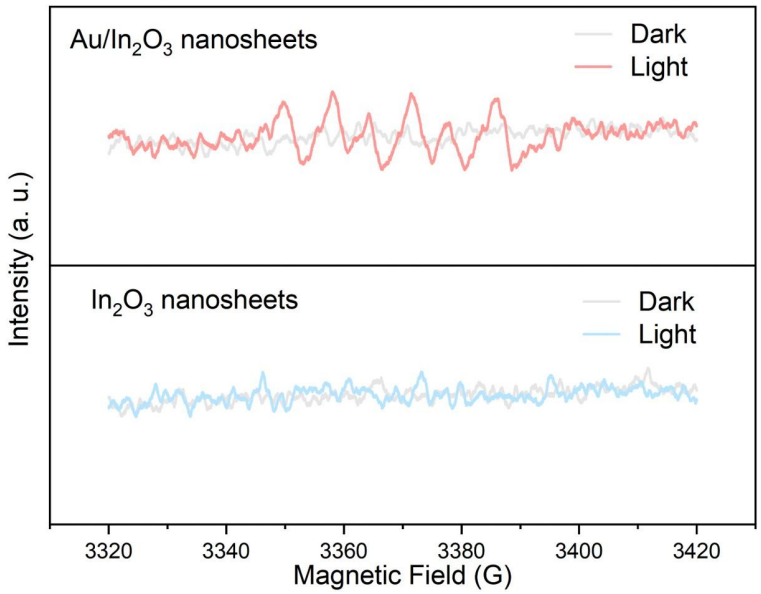

Fig. S17. *In situ* EPR spectra for the detection of $\cdot O_2^-$ under illumination of the Au/In_2O_3 nanosheets and the In_2O_3 nanosheets.

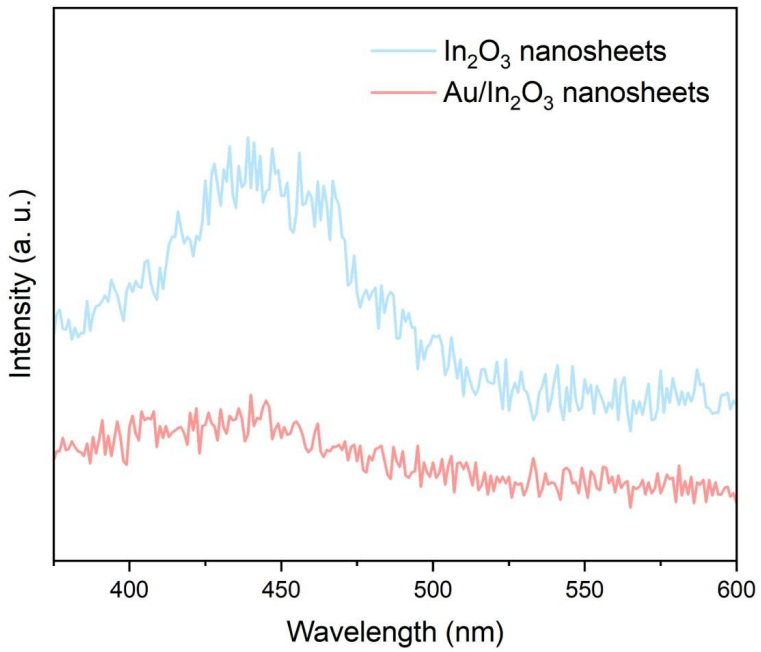

Fig. S18. PL spectra of the Au/In_2O_3 nanosheets and the In_2O_3 nanosheets.

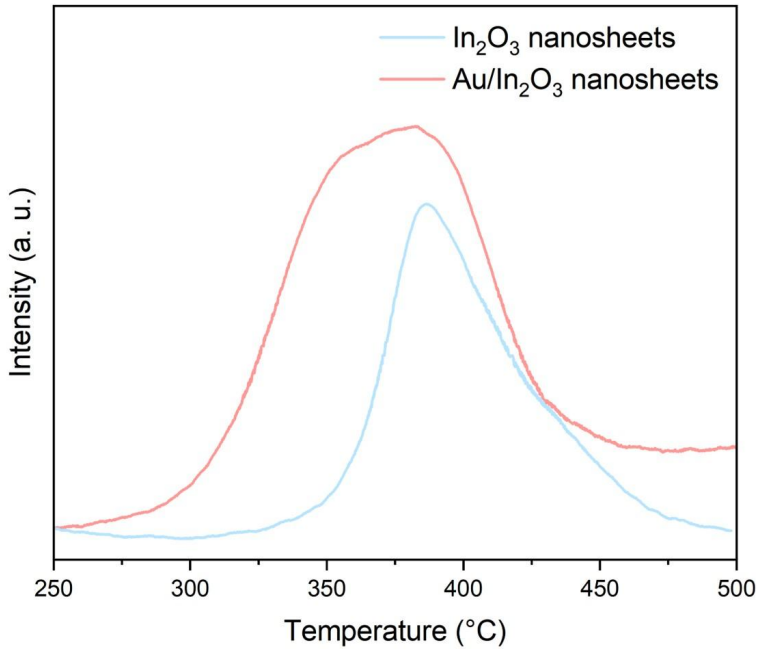

Fig. S19. CO_2-TPD measurements for the Au/In_2O_3 nanosheets and the In_2O_3 nanosheets.

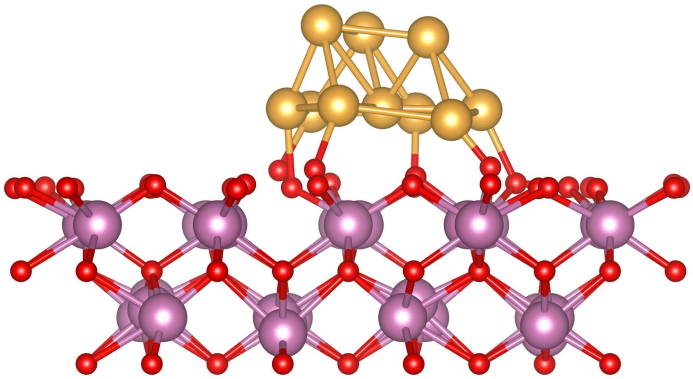

Fig. S20. The relaxed Au/In_2O_3 nanosheet slab model.

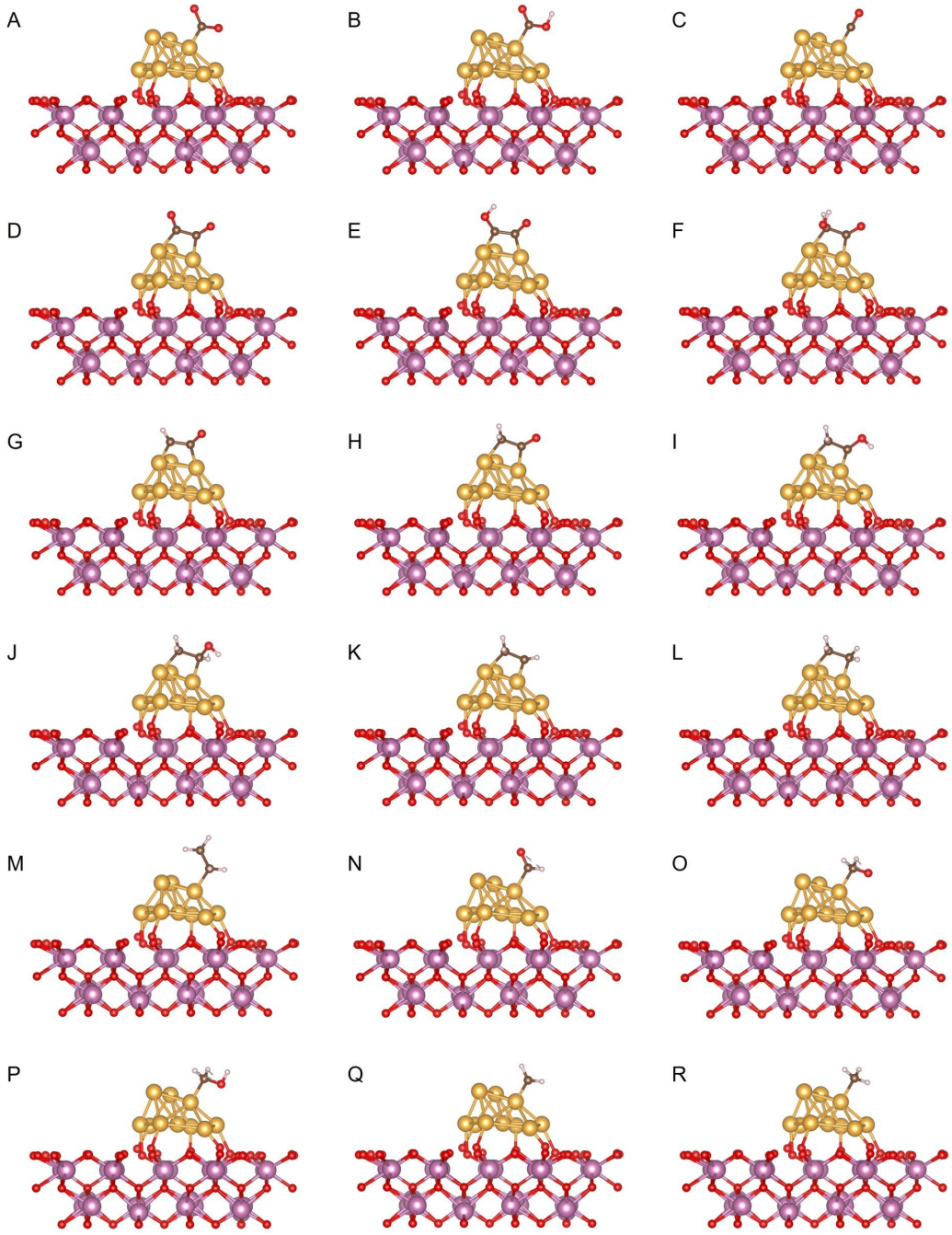

Fig. S21. (A) *CO_2, (B) *COOH, (C) *CO, (D) *OCCO, (E) *OCCOH, (F) *OCCHOH, (G) *OCCH, (H) *$OCCH_2$, (I) *$COHCH_2$, (J) *$CHOHCH_2$, (K) *$CHCH_2$, (L) *CH_2CH_2, (M) *CH_2CH_3, (N) *CHO, (O) *CH_2O, (P) *CH_2OH, (Q) *CH_2 and (R) *CH_3 adsorbed on the Au/In_2O_3 nanosheet slab. The yellow, purple, red, brown and white spheres represent Au, In, O, C and H atoms, respectively.

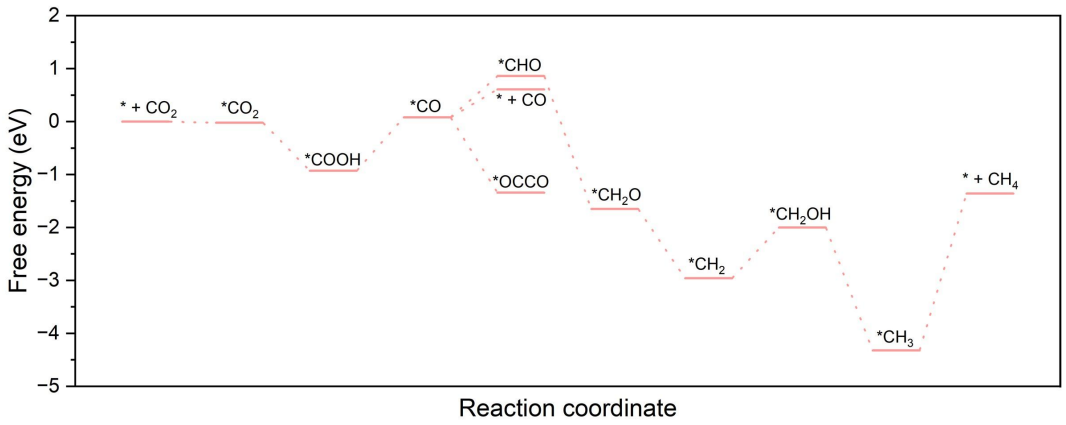

Fig. S22. Gibbs free energy profiles of the CO_2RR to CO and CH_4 over the Au/In_2O_3 nanosheet slab.

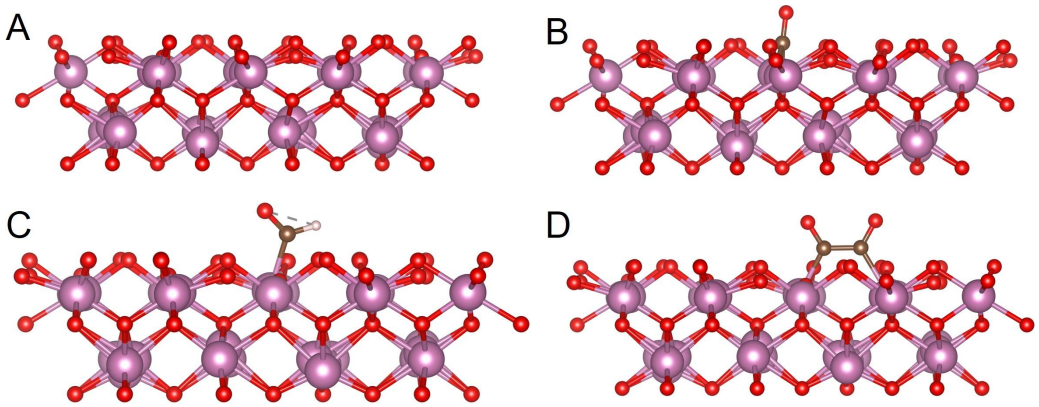

Fig. S23. (A) The relaxed In_2O_3 nanosheet models of slab. (B) *CO, (C) *CHO and (D) *OCCO adsorbed on the In_2O_3 nanosheet slab, respectively. The purple, red, brown and white spheres represent In, O, C and H atoms, respectively.

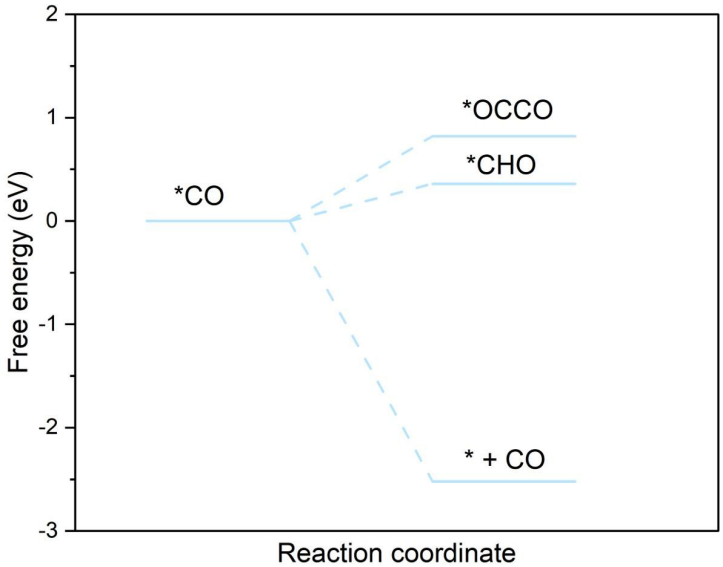

Fig. S24. Gibbs free energy profiles of the In_2O_3 nanosheet slab.

Table S1. Elemental compositions of the samples

Sample	Mass fraction of Au (%)
0.81Au/In_2O_3 nanosheets	0.81
1.57Au/In_2O_3 nanosheets	1.57
2.18Au/In_2O_3 nanosheets	2.18

Table S2. Structural parameters of the Au foil and the Au/In_2O_3 nanosheets obtained from the EXAFS fitting analysis. (S_0^2=0.87)

Sample	Path	CN	R(Å)	σ^2*10^{-3} (Å^{-2})	ΔE_0 (eV)	R-factor (%)
Au foil	Au-Au	12	2.86	/	/	/
Au/In_2O_3 nanosheets	Au-Au	9.96±0.55	2.85±0.02	8.1±0.5	4.20±0.86	1.47

CN: coordination number; R: distance between absorber and backscatter atoms; σ^2: Debye-Waller factors; ΔE_0: inner potential correction; R-factor: indicative of fitting goodness. The accuracies of the above parameters are estimated as CN, ±20%; R, ±1%; σ^2, ±20%; ΔE_0, ±20%.

Table S3. Structural parameters of the Au/In_2O_3 nanosheets and the In_2O_3 nanosheets obtained from the EXAFS fitting analysis. (S_0^2=0.98)

Sample	Path	CN	R(Å)	σ^2*10^{-3} (Å^{-2})	ΔE_0 (eV)	R-factor (%)
Au/In_2O_3 nanosheets	In-O1	4.0±0.2	2.15±0.01	3.0±0.7	9.5±0.3	1.70
	In-O2	2.0±0.3	2.24±0.04	9.3±2.6		
	In-In	5.8±0.6	3.38±0.01	7.5±0.6		
In_2O_3 nanosheets	In-O1	4.0±0.1	2.15±0.01	3.3±0.9	9.7±0.2	0.52
	In-O2	1.9±0.2	2.23±0.02	10.00±1.7		
	In-In	5.6±0.4	3.39±0.01	6.4±2.7		

CN: coordination number; R: distance between absorber and backscatter atoms; σ^2: Debye-Waller factors; ΔE_0: inner potential correction; R-factor: indicative of fitting goodness. The accuracies of the above parameters are estimated as CN, ±20%; R, ±1%; σ^2, ±20%; ΔE_0, ±20%.

Table S4. Comparison of the performances with other catalysts for photocatalytic CO_2 reduction to C_2H_6.

Sample	C_2H_6 evolution rates ($\mu mol\ g^{-1}\ h^{-1}$)	Electron selectivity (%)	Product selectivity (%)	Reference
Au/In_2O_3 nanosheets	**46.3**	**85.1**	**71.9**	**This work**
PCCN-10	99.1	/	80.3	10
AuCu-NU-1000	69.9	71.1	/	11
Cu-CuTCPP/C_3N_4	18.5	/	44	12
PQD-PCN-6'	16.3	64.4	/	13
Au-CeO_2	11.1	93.1	65.3	14
Z_3N-TC	10.27	/	14.5	15
Au-$Bi_4Ti_3O_{12}$	2.58	70	/	16
ZSM-5@NiV_2Se_4	1.85	90.1	77.2	17
Au_1/RP	1.32	/	96	18

Table S5. The evolution rates of C_2H_6 during the photoconversion process under room temperature and ambient pressure. The 'n.d.' in the table refers to 'not detected'.

Products	Dark	No catalyst	In Ar
CO ($\mu mol\ g^{-1}\ h^{-1}$)	n.d.	n.d.	n.d.
CH_4 ($\mu mol\ g^{-1}\ h^{-1}$)	n.d.	n.d.	n.d.
C_2H_4 ($\mu mol\ g^{-1}\ h^{-1}$)	n.d.	n.d.	n.d.
C_2H_6 ($\mu mol\ g^{-1}\ h^{-1}$)	n.d.	n.d.	n.d.

Table S6. The electron energy and the Gibbs free energy (eV) correction of the calculated species.

Species	E_{elec}	ΔG_{corr}	G
CO_2(g)	-22.95	-0.25	-23.20
H_2O(l)	-14.22	-0.001	-14.22

CH_4(g)	-24.04	0.71	-23.32
H_2(g)	-6.76	-0.05	-6.80
C_2H_4(g)	-31.97	0.78	-31.19
C_2H_6(g)	-40.50	1.39	-39.11
CO(g)	-0.39	-14.78	-15.17
Au/In_2O_3	-485.26	0	-485.26
$*CO_2@Au/In_2O_3$	-508.68	0.20	-508.48
$*COOH@Au/In_2O_3$	-513.27	0.49	-512.78
$*CO@Au/In_2O_3$	-501.16	0.21	-500.96
$*OCCO@Au/In_2O_3$	-517.93	0.38	-517.55
$*OCCOH@Au/In_2O_3$	-521.23	0.66	-520.57
$*OCC(H)OH@Au/In_2O_3$	-525.20	0.97	-524.23
$*OCCH@Au/In_2O_3$	-515.31	0.50	-514.81
$*OCCH_2@Au/In_2O_3$	-518.51	0.85	-517.65
$*COHCH_2@Au/In_2O_3$	-521.45	1.16	-520.29
$*C(H)OHCH_2@Au/In_2O_3$	-524.86	1.47	-523.39
$*CHCH_2@Au/In_2O_3$	-512.76	1.01	-511.75
$*CH_2CH_2@Au/In_2O_3$	-518.41	1.22	-517.19
$*CH_2CH_3@Au/In_2O_3$	-523.11	1.64	-521.47
$*CHO@Au/In_2O_3$	-504.00	0.42	-503.58
$*HCHO@Au/In_2O_3$	-510.18	0.69	-509.49
$*CH_2OH@Au/In_2O_3$	-515.24	1.05	-514.20
$*CH_2@Au/In_2O_3$	-503.04	0.62	-502.42

*CH_3@Au/In_2O_3	-509.01	0.87	-508.14
In_2O_3	-459.51	0	-459.51
*CO@In_2O_3	-472.33	0.18	-472.15
*OCCO@In_2O_3	-486.81	0.36	-486.45
*CHO@In_2O_3	-475.62	0.39	-475.23

References

1. G. Kresse and J. Furthmüller, *Computational Materials Science*, 1996, **6**, 15-50.

2.J. P. Perdew, K. Burke and M. Ernzerhof, *Physical Review Letters*, 1996, **77**, 3865-3868.

3.V. L. Deringer, A. L. Tchougréeff and R. Dronskowski, *The Journal of Physical Chemistry A*, 2011, **115**, 5461-5466.

4.R. Dronskowski and P. E. Bloechl, *The Journal of Physical Chemistry*, 1993, **97**, 8617-8624.

5.R. Nelson, C. Ertural, J. George, V. L. Deringer, G. Hautier and R. Dronskowski, *Journal of Computational Chemistry*, 2020, **41**, 1931-1940.

6.S. Maintz, M. Esser and R. Dronskowski, *ACTA PHYSICA POLONICA B*, 2016, **47**, 1165-1175.

7.S. Maintz, V. L. Deringer, A. L. Tchougréeff and R. Dronskowski, *Journal of Computational Chemistry*, 2016, **37**, 1030-1035.

8.S. Maintz, V. L. Deringer, A. L. Tchougréeff and R. Dronskowski, *Journal of Computational Chemistry*, 2013, **34**, 2557-2567.

9.J. K. Nørskov, J. Rossmeisl, A. Logadottir, L. Lindqvist, J. R. Kitchin, T. Bligaard and H. Jónsson, *The Journal of Physical Chemistry B*, 2004, **108**, 17886-17892.

10.Z. Chen, G. Ding, Z. Wang, Y. Xiao, X. Liu, L. Chen, C. Li, H. Huang and G. Liao, *Advanced Functional Materials*, 2025, **35**, 2423213.

11.D. Chen, B. Chu, F. Li, Y.-T. Zheng, Y. Lu, B. Shao, L. Li, N.-Y. Huang and Q. Xu, *Journal of the American Chemical Society*, 2025, **147**, 22705-22713.

12.S. Xie, Y. Li, B. Sheng, W. Zhang, W. Wang, C. Chen, J. Li, H. Sheng and J. Zhao, *Applied Catalysis B: Environmental*, 2022, **310**, 121320.

13.J. Xu, M. Chong, W. Li, E. Zhu, H. Jin, L. Liu, Y. Ren and Y. Zhu, *Chem*, 2025, **11**, 102295.

14.J. Ji, R. Li, H. Zhang, Y. Duan, Q. Liu, H. Wang and Z. Shen, *Applied Catalysis B: Environmental*, 2023, **321**, 122020.

15.B. Ni, H. Jiang, W. Guo, Q. Xu and Y. Min, *Applied Catalysis B: Environment and Energy*, 2022, **307**, 121141.

16.G. Huang, D. He, Z. Zhou, W. Yan, Y. Pan, J. Hu, J. Zhu, X. Zhang, Y. Dong, J. Xu and X. Jiao, *Science China Materials*, 2025, DOI: 10.1007/s40843-025-3464-4.

17.Y. Tian, R. Wang, S. Deng, Y. Tao, W. Dai, Q. Zheng, C. Huang, C. Xie, Q. Zeng, J. Lin and H. Chen, *Nano Letters*, 2023, **23**, 10914-10921.

18.H. Ou, G. Li, W. Ren, B. Pan, G. Luo, Z. Hu, D. Wang and Y. Li, *Journal of the American Chemical Society*, 2022, **144**, 22075-22082.